

Chemically Induced Ferroic-like Phase and Collective Chemotaxis in an Active Swarm

Changjin Wu,[‡] Yaxin Huang,[‡] Binglin Zeng,[‡] Jingyuan Chen, Chun Hung Chu, Mingcheng Yang, Ho Cheung Shum, and Jinyao Tang*



Cite This: *J. Am. Chem. Soc.* 2025, 147, 40225–40235



Read Online

ACCESS |



Metrics & More

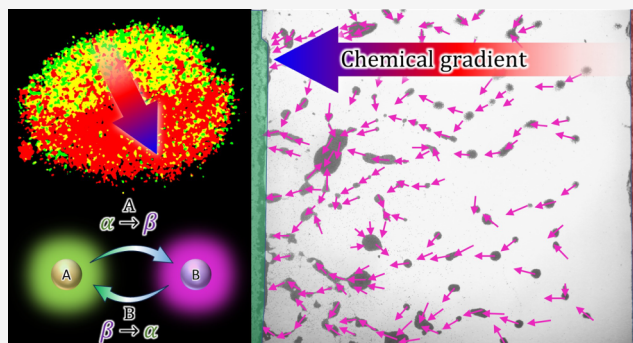


Article Recommendations



Supporting Information

ABSTRACT: Amplification of weak chemical signals through intracellular cascade networks is crucial for long-range cohesive migration in biological processes, such as embryogenesis and cancer metastasis. While this capability has transformative potential for synthetic systems in precision medicine and adaptive materials, the lack of cascade communication in artificial matter has been a significant barrier. This study demonstrates that a binary active colloid mixture, mediated by a chemical reaction, forms a simple chemical reaction network capable of self-organizing into polarized dynamic swarms, dramatically enhancing chemical amplification. By applying the classical Ising model, we rationalize the self-polarization with increasing chemical activity, drawing an analogy to ferroic materials in the chemically polarized active phase. Under optimal conditions, these “ferrochemical” swarms can amplify weak chemical gradients by over 10^4 times, resulting in exceptional chemical sensitivity and remarkable long-range collective chemotaxis. As a proof of concept, we demonstrate the application of silver-doped active swarms to enhance antibacterial efficacy, showcasing a chemotactic swarm that effectively combats dental biofilm growth on human teeth.



1. INTRODUCTION

Collective chemotaxis,^{1–3} the orchestrated movement of cells and bacteria in response to chemical gradients, is a fundamental process underpinning many biological functions, including immune responses, embryonic development, and cancer metastasis.^{1,4} At the core of this intricate phenomenon lies the remarkable ability of living organisms to amplify weak chemical signals through intracellular signaling cascade networks, enabling both high sensitivity and specificity to their surrounding environments.^{5–7}

Fundamentally, the cellular signaling pathway is an intricate chemical reaction network, allowing chemical amplification within this network. In contrast, materials at thermodynamic equilibrium are unable to perform this function, as it violates the second law of thermodynamics. Recent developments in active colloids, which operate far from thermodynamic equilibrium,^{8–10} have opened new possibilities that, in principle, enable novel emergent functions previously unique to living organisms. Synthetic active matters have demonstrated chemotaxis ability, where enzymes or active colloids track chemical signals by directly reacting with the related substrates.^{11–14} These advancements herald significant potential for biomedical applications, including targeted drug delivery and precise noninvasive surgery.⁸ However, due to the lack of signaling cascade amplification,^{15,16} the chemotactic

ability of synthetic colloids is substantially weaker compared to their biological counterparts, requiring orders of magnitude stronger chemical gradients than those present in physiological environments to induce noticeable chemotaxis. Despite extensive studies that have demonstrated advanced applications of synthetic colloids in diverse physiological environments, such as bladder^{17,18} and gastrointestinal tract,^{19,20} a general chemotactic mechanism for targeted biomedicine has yet to be established.

In this work, we focus on chemotactic systems in which gradients of diffusible chemical mediators govern the directional movement of active ensembles. Inspired by ferromagnetic/ferroelectric materials, where individual dipole moments align to amplify external fields, we discovered a chemically polarized active phase in a binary active colloid mixture composed of chemically active Zinc Germanate (ZGO) nanorods and Sulfonated Polystyrene (SPS) microbeads. These colloids react chemically with each other and self-

Received: June 14, 2025

Revised: September 23, 2025

Accepted: September 24, 2025

Published: October 1, 2025



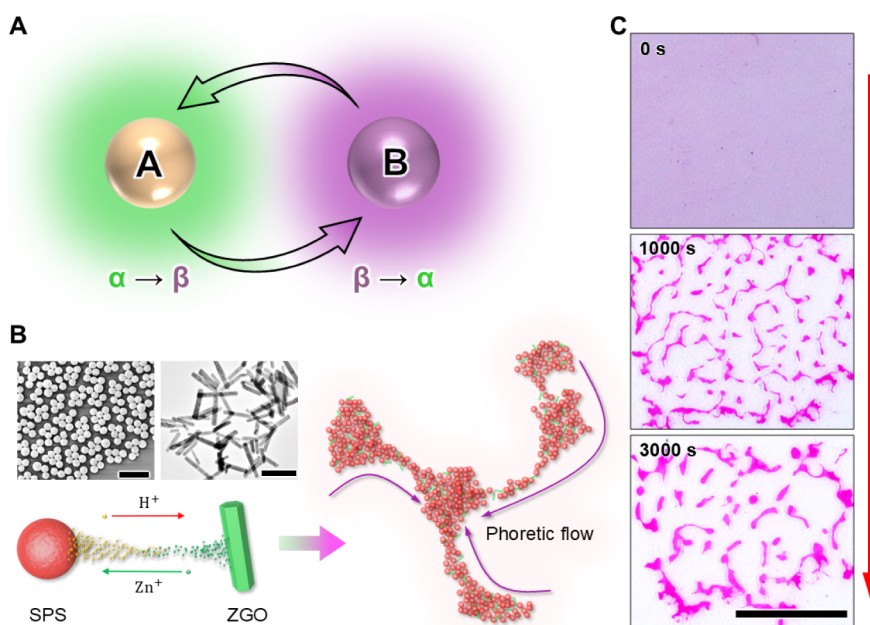


Figure 1. Emergence of the ZGO-SPS active swarm. A) Conceptual illustration of exchange coupling between two chemically active particles, A and B, which exchange chemicals α and β . B) The exchange of protons and Zn^{2+} between SPS and ZGO induces nonreciprocal coupling, which promotes the formation of ZGO-SPS active clusters via self-diffusiophoresis. Insets show electron microscope images of SPS and ZGO particles, respectively. C) Snapshots of phase evolution showing the formation of ZGO-SPS active clusters. Scale bars: 5 μm (B, left), 200 nm (B, right), 1 mm (C).

organize into highly polarized, dynamic clusters, exhibiting remarkable chemical amplification and significantly enhanced chemotactic capability. Importantly, as a conceptual metaphor, the observed self-polarization state exhibits certain characteristics similar to ferroic ordering. However, due to the nonequilibrium conditions and the nonconserved nature of chemical polarization, this ferroic-like order fundamentally differs from that of classical ferroic phases. The classical Ising model is applied to this active system, predicting a second-order phase transition at a critical reactivity, which is corroborated by experimental results. These self-polarized clusters create local pH gradients that align with external gradients, analogous to magnetic domains aligning with external fields, amplifying chemical gradients over 10^4 times and resulting in highly sensitive chemotaxis. We term this new material state, characterized by strong chemical reaction dissipation, the “ferrochemical” phase, emphasizing its gigantic chemical signal amplification ability.

Although this chemical dipole framework does not intend to universally describe all forms of chemotaxis, such as those mediated by multivalent or direct-contact mechanisms,^{21–23} it provides a general quantitative tool for analyzing systems where chemical gradient sensing and amplification are central. To demonstrate its applicability, we utilized silver-doped swarms for targeted chemotaxis in dental biofilm control, significantly enhancing sterilization by actively tracking the acid produced by human oral bacteria. The sulfonate groups of SPS provide a tunable platform for cation exchange and proton release, establishing dynamic chemical gradients in concert with those of ZGO nanorods. The interplay of ion-exchange kinetics and surface chemical functionality is directly mapped onto the emergent ferrochemical phase behavior, revealing new opportunities for amplified chemical sensing,^{6,24} adaptive supramolecular assembly,^{25,26} and active therapeutic delivery^{11,13} in complex biological environments.

2. RESULTS AND DISCUSSION

2.1. Exchange Coupling-Induced Active Swarm and Self-Polarization. Our experimental system parallels our previously developed ion-exchange-enabled active colloidal system.²⁷ In this work, ZnO is replaced with ZGO, which prevents the structural degradation of ZnO after Ag doping and enables the formation of polarized clusters with SPS rather than core-shell ZnO-SPS clusters. As conceptually illustrated in Figure 1A, two chemically active particles, A and B, communicate via exchange interactions. Specifically, particle A converts chemical α to β , while particle B converts β back to α , enabling mutual sensing of chemical gradients and establishing communication. In this study, chemical communication is achieved through ion-exchange interactions between ZGO and SPS, where protons are donated from SPS to ZGO, while ZGO donates Zn^{2+} back to SPS to maintain charge neutrality (Figure 1B). The SPS microbeads have an average diameter of 1 μm , while the ZGO nanorods are approximately 200 nm in length (see Supporting Information for the synthesis process and characterization of the particles). Similar to our previous report,²⁷ this exchange coupling is nonreciprocal and induces long-range attraction/repulsion via self-diffusiophoresis. Non-equilibrium systems with nonreciprocally coupled matter have received significant interest in recent years. Collective behaviors of these systems have been investigated both theoretically^{28,29} and experimentally.^{30–32} In our system, the nonreciprocal exchange of chemicals results in phase separation into dilute and condensed phases, which gradually coarsen into larger, dynamic clusters, as shown by the labyrinth-like patterns in Figure 1C and Movie S1. A typical power-law dependence of the cluster size on the evolution time can be observed in the Supporting Information. Notably, unlike colloidal assembly driven by short-range interactions in equilibrium,^{33–35} such as electrostatic and hydrophobic interactions, the active colloidal clusters formed by long-

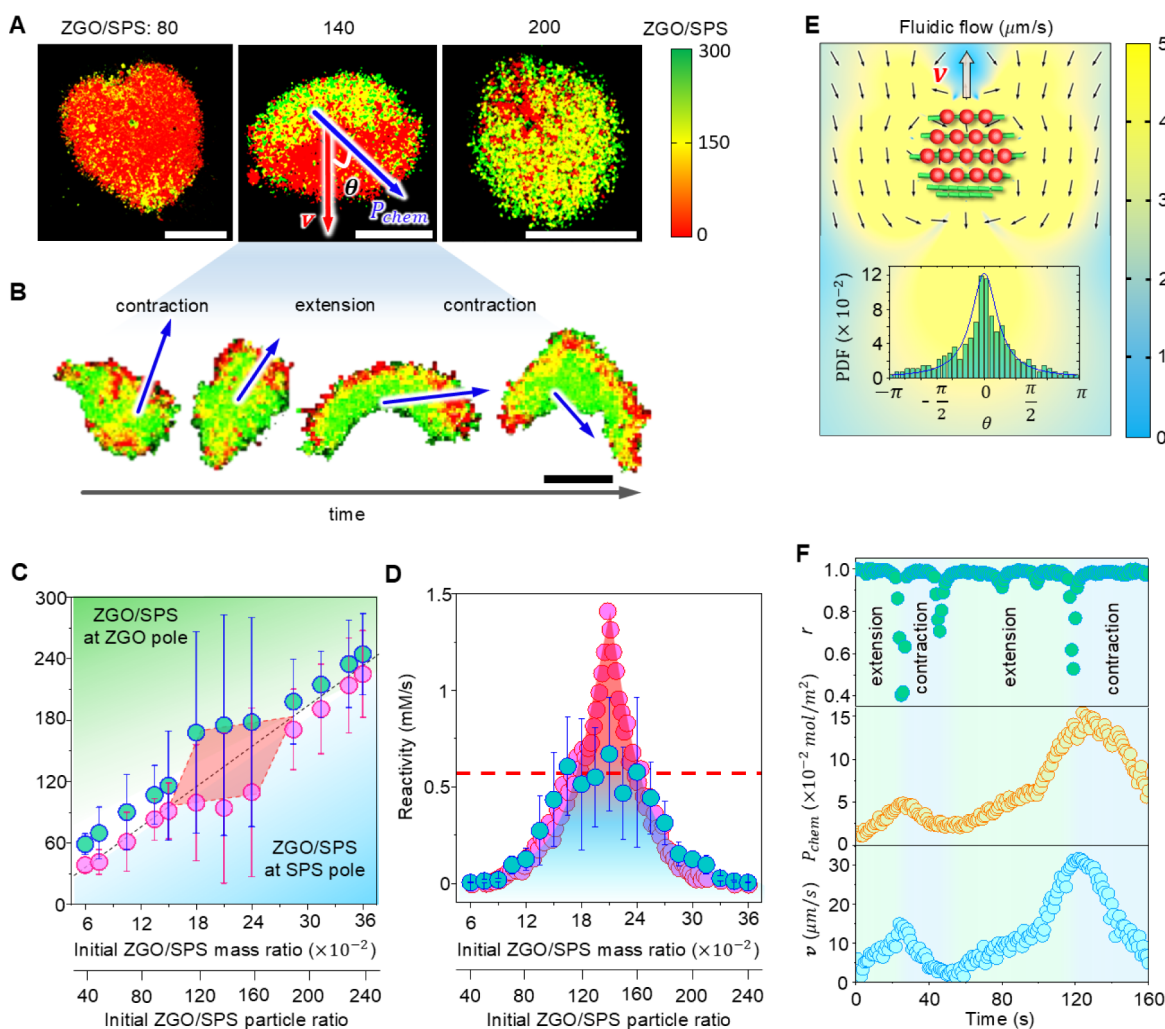


Figure 2. Self-polarization of the ZGO-SPS active cluster. A) Dual-color fluorescence images reveal the local composition in ZGO-SPS clusters with initial ZGO/SPS ratios of 80, 140, and 200. The polarization density P_{chem} , propulsion velocity v , and deviation angle θ are marked on the image. The vectors for v and P_{chem} are defined from the cluster centroid; P_{chem} is quantified based on the proton concentration field as described in the Supporting Information. B) Sequential snapshots show a polarized cluster's dynamic contraction and extension. The blue arrows indicate the instantaneous polarization vector P . The ZGO/SPS ratio = 140. The apparent dynamic change of fluorescence with the same ZGO/SPS ratio is due to the overlap of two different fluorescence signals. C) Averaged ZGO/SPS ratio at ZGO and SPS poles for clusters with different initial compositions, where the red diamond area indicates the forbidden zone associated with self-polarization. The error bars are calculated from clusters in 3 parallel experiments. D) The relationship between the reaction rate and relative composition. The intrinsic reaction rate (pink points) peaks at 140. The active cluster reactivity (blue points) plateaus and does not pass a critical threshold (red dashed line). The error bars are calculated from 5 parallel experiments. E) Simulated fluidic flow generated by a polarized cluster composed of ZGO (green rods) and SPS (red beads) shows propulsion along the polarization. The black arrows represent the flow directions. The inset shows the experimental PDF of the deviation angle θ of different clusters. F) Correlation coefficient r (top) of the amplitude of polarization density P (middle) and velocity v (bottom) during the motion of the polarized cluster in Movie S2. The green and blue backgrounds highlight the extension and contraction. Scale bars: 100 μm (A); 100 μm (B).

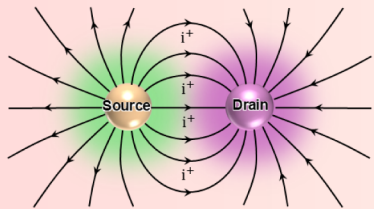
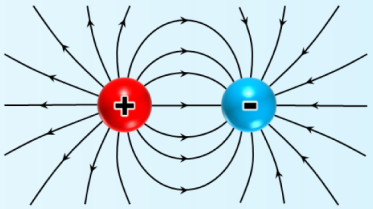
range phoretic interactions are highly dynamic, undergoing continuous reconfiguration and internal rearrangement.^{36–38}

Importantly, as the exchange reaction occurs between two active colloid species, the overall reaction rate can be modulated by adjusting the relative composition of the cluster. To distinguish the colloid composition within the active clusters and study its dynamic evolution, we labeled ZGO (positively charged, zeta potential ~ 25 mV) with fluorescein (green) and SPS (negatively charged, zeta potential ~ -35 mV) with rhodamine (red), respectively. The dyes adsorbed on the surfaces of the particles were confirmed to have no significant effect on the behavior of the colloids. Details of the dye-labeling method are provided in the Supporting

Information. Subsequently, we examined the collective behaviors and dynamic composition of the colloids at specific ZGO/SPS particle and mass ratios using fluorescence microscopy (see Supporting Information for a detailed process). Note that the colloid composition can be equivalently determined by either the particle ratio or the mass ratio of ZGO/SPS. In this paper, the particle ratio is used unless otherwise specified. As shown in Figure 2A, both the morphology and composition of the formed clusters vary dramatically with cluster composition.

When the cluster predominantly comprises one colloid species (ZGO/SPS particle ratio above 180 or below 100), the exchange reaction is slow, resulting in relatively spherical

Table 1. Comparison of Chemical Dipole to Electric Dipole and Corresponding Variables

Chemical Dipole	Electric Dipole
	
Chemical Concentration of species i : C_i	Charge Density: ρ_E
Chemical Potential of Species i : μ_i	Electric Potential: ϕ
Chemical Dipole: $\mathbf{p}_{chem} = \int_V C_i (\mathbf{r} - \mathbf{r}_0) d^3\mathbf{r}$	Electric Dipole: $\mathbf{p} = \int_V \rho_E (\mathbf{r} - \mathbf{r}_0) d^3\mathbf{r}$
Chemical Polarization Density: $\mathbf{P}_{chem} = \frac{\mathbf{p}_{chem}}{V}$	Polarization Density: $\mathbf{P} = \frac{\mathbf{p}}{V}$
Chemical Energy Density: $\mu_{chem} = C_i \mu_i$	Electric Energy Density: $\mu_E = \rho_E \phi$
Chemical Field: $\mathbf{h}_{chem} = -\nabla \mu_i = -RT \frac{\nabla C_i}{C_i}$	Electric Field: $\mathbf{E} = -\nabla \phi$
Alignment Energy: $U = -\mathbf{p}_{chem} \cdot \mathbf{h}_{chem}$	Alignment Energy: $U = -\mathbf{p} \cdot \mathbf{E}$
Chemical Susceptibility: $\chi_{chem} = \frac{\mathbf{P}_{chem}}{\varepsilon_{chem} \mathbf{h}_{chem}} = \frac{\mathbf{P}_{chem}}{\mathbf{P}_{solvent}}$	Electric Susceptibility: $\chi_e = \frac{\mathbf{P}}{\varepsilon_0 \mathbf{E}} = \frac{\mathbf{P}}{\mathbf{P}_{vacuum}}$

clusters. The distribution of the two colloid species within the clusters resembles a random mixture, and overall cluster dynamics are weak. In contrast, at a ZGO/SPS ratio of around 140, a distinct polarized cluster (middle image in Figure 2A) forms, with clearly identifiable ZGO-enriched and SPS-enriched poles. However, at ratios below 80 or above 200, the reactivity sharply decreases due to the depletion of one reactant, and stable polarized clusters do not form. The presence of numerous internal active particles makes these polarized clusters highly dynamic, constantly changing morphology and migrating rapidly in solution. As shown in Figure 2B and Movie S2, the polarized cluster exhibits spring-like morphing with cyclic extension and contraction, resulting in pronounced fluctuations in reactivity. This compositional instability can be visualized by gradually varying the overall cluster composition while observing the local composition at both ZGO and SPS poles. As shown in Figure 2C, a forbidden zone, shaded in red, indicates the microscale phase separation within the clusters that partially separates ZGO and SPS, while strong fluctuations, as indicated by the prominent standard deviation, are also a distinct feature of this region.

The relationship between activity and composition can be established to rationalize this microscale phase separation. The intrinsic chemical reaction rate was measured by mixing the ZGO and SPS colloids under constant agitation, which prevented cluster polarization by disrupting phase separation. As shown in Figure 2D, a volcano-like relationship is observed between composition and reactivity, with the reaction rate peaking at a ZGO/SPS ratio near 1:40. Notably, due to the formation of polarized clusters, the optimal reaction rate is not achieved within the active clusters. The overall system reaction rate is limited to below a critical value (highlighted by the red dashed line) in both the ZGO-rich and SPS-rich regions, strongly suggesting that this microscale phase transition is regulated by cluster activity. However, beyond the forbidden zone, although the low reaction rates allow cluster formation, no obvious polarization can be observed (Figure 2C).

Since particle–particle interactions are mediated by chemical gradients, we propose quantifying the polarization of active clusters using the mediator's concentration.

Specifically, in the ZGO/SPS system, H^+ and Zn^{2+} are the mediating chemicals, allowing the chemical polarization of the active cluster to be defined as $\mathbf{P}_{chem}^{[H^+]} = \frac{1}{V} \int_V [H^+]_r (\mathbf{r} - \mathbf{r}_0) d^3\mathbf{r}$ or $\mathbf{P}_{chem}^{[Zn^{2+}]} = \frac{1}{V} \int_V [Zn^{2+}]_r (\mathbf{r} - \mathbf{r}_0) d^3\mathbf{r}$, where \mathbf{r} is the position vector and \mathbf{r}_0 is the location vector of the cluster's center of mass. Since the total amount of the two exchange reagents is always balanced by stoichiometry, these two chemical fields are conjugated, such that $\mathbf{P}_{chem}^{[H^+]} = -2\mathbf{P}_{chem}^{[Zn^{2+}]}$, allowing us to use a single reactant to quantify the polarization of the cluster. For simplicity in calculation and measurement, we define polarization as $\mathbf{P}_{chem} = \mathbf{P}_{chem}^{[H^+]}$ (see Supporting Information for details). With this definition, the chemical dipole of the cluster points from the proton sink (ZGO pole) to the proton source (SPS pole), as shown in the middle image of Figure 2A. This chemical dipole generates a diffusio-phoretic flow, resulting in overall self-propulsion of the cluster along its polarization, \mathbf{P}_{chem} , as demonstrated by the simulation in Figure 2E (see Supporting Information for the simulation details). We analyzed the deviation angle θ between \mathbf{P}_{chem} and \mathbf{v} over various clusters, and the resulting probability density function (PDF) confirms that the polarized cluster indeed self-propels along its polarization (inset of Figure 2E). In addition, the correlation coefficient (r) between the amplitude of \mathbf{P}_{chem} and \mathbf{v} is mostly close to 1, indicating the propulsion force not only aligns but also scales with the cluster polarization (Figure 2F).

Particularly, the defined \mathbf{P}_{chem} is directly analogous to the magnetization order parameter in ferromagnetic systems.³⁹ Here, a nonzero value of \mathbf{P}_{chem} indicates the onset of a collectively polarized, “ferrochemical” state. The chemical susceptibility describes how sensitively the cluster polarization responds to an applied proton gradient, in analogy to the susceptibility⁴⁰ of ferroic materials. This quantitative approach allows us to identify the emergence of collective behavior rigorously and to measure the amplification of the chemotactic response in active clusters.

2.2. Ising Model for Active Phase Transition. While the chemical reactions involved in ion-exchange systems are simple, the detailed interactions between two reactive species

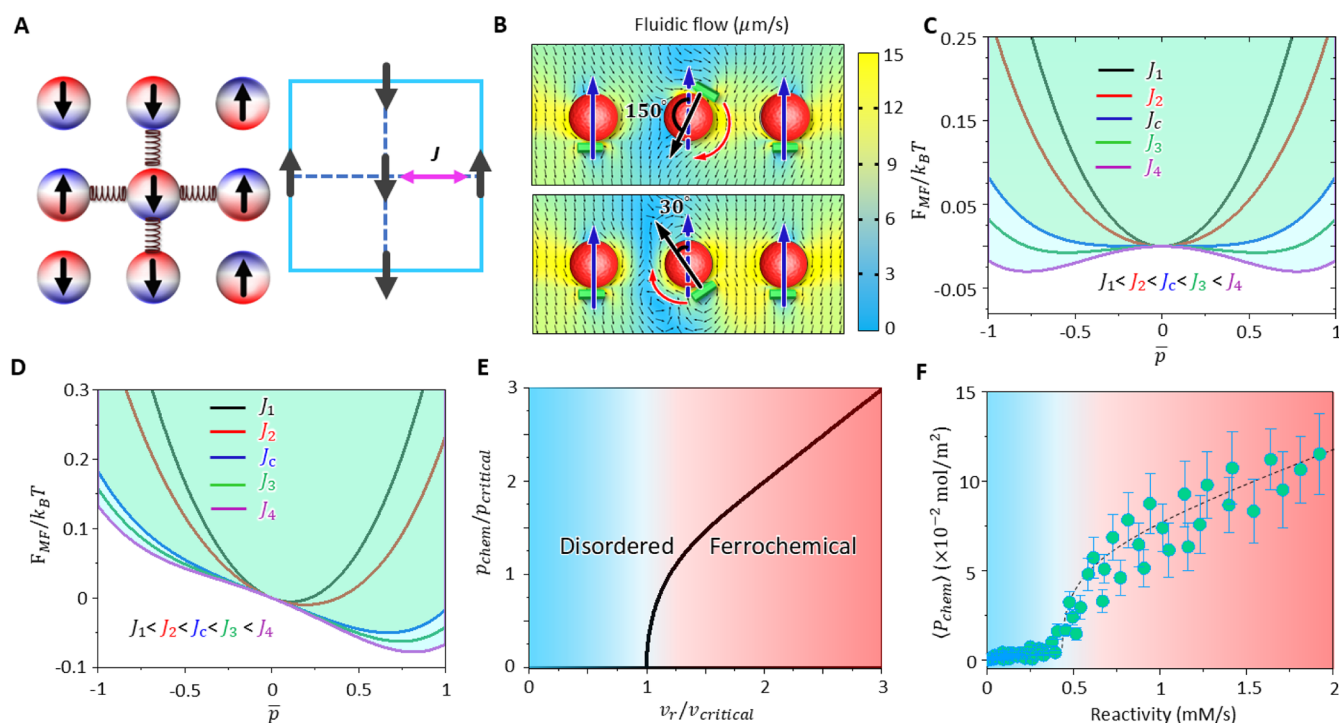


Figure 3. Active phase transition as described by the Ising model. A) Schematic diagram showing the Ising model-like active cluster composed of interacting dipole pairs with coupling strength J . B) Simulation result of the flow field of interacting ZGO (green rod)–SPS (red bead) pairs. The exchange reaction generates a fluidic flow, leading to parallel alignment. The red arrows indicate the flow direction. C, D) Effective free energy tuned by the exchange strength J without (C) and with (D) an external field. Black, red, blue, green, and purple lines correspond to increasing J_1 to J_4 with $J_1 < J_2 < J_3 < J_4$, respectively. E) Dependence of overall polarization on reaction rate as predicted by the Ising model without an external field. The blue and red backgrounds highlight the transition from the disordered to the ferrochemical phase. F) Experimental results of the dependence of the mean polarization density $\langle P \rangle$ of ZGO–SPS clusters on reactivity, showing a phase transition at critical reactivity. The error bars were from 5 parallel experiments.

are remarkably intricate, encompassing complex long-range attraction–repulsion forces, nonreciprocity, as well as quorum-sensing ability, as we showed earlier.²⁷ Due to these complexities, constructing an exact model with detailed interaction mechanisms inevitably results in a large parameter space and complicated phase behavior.

On the other hand, in recent years, many of these fascinating new nonequilibrium ingredients have been incorporated into minimal models for active matter systems,^{41–46} where many can be adapted to reproduce the phenomena observed in our system. For example, Agudo-Canalejo et al. considered the binary mixture of two chemically interacting species, where the interactions are generally nonreciprocal.⁴¹ They demonstrated that such nonreciprocal interactions can give rise to phase separation, as well as self-polarized clusters, closely mirroring our experimental observations. Subsequently, the same group extended this framework by formulating an active Cahn–Hilliard model, in which asymmetric pairwise interactions between active particles govern both macroscopic phase separation and the emergence of global polar order.⁴³ Meanwhile, Speck et al. explored systems of active Brownian particles with repulsive interactions, mapping their behavior onto that of passive systems. This mapping enabled the derivation of a Clausius–Clapeyron-like equation to predict phase separation in active systems with an intuitive thermodynamic analogy.⁴²

With these prior works, we aim to adopt a further minimized model, drawing an analogy to the traditional passive thermodynamic theory of ferroic phase transition, allowing

for a more intuitive understanding of the system’s self-polarization and chemical amplification ability. However, it is important to note that this naive analogy is far from accurate and is used solely to facilitate conceptual understanding, as more accurate models are already available in the literature.

Drawing an analogy to the ferroelectric phase transition, we treat the chemical dipole in our system as analogous to an electric dipole, with the corresponding variables and interactions summarized in Table 1. These analogies may provide a general theoretical framework for understanding chemotactic materials. Importantly, the chemical susceptibility is defined as the ratio of the polarization within the material to the polarization observed in a free solution, thereby quantifying the system’s ability to amplify chemical gradients. Within this theoretical framework, many phase transition models, such as the Ising model,⁴⁷ can be adopted to understand active swarms. By considering the interactions between neighboring dipoles and the influence of external fields, these models can provide insights into phase transitions and domain formation, even though they are typically used to describe systems at thermodynamic equilibrium. Given that our system exhibits a phase transition reminiscent of ordering in equilibrium models, we use the classical Ising model here as a conceptual tool to intuitively illustrate the emergence of polarization arising from local interactions. We acknowledge that this approach does not capture the full complexity of nonreciprocal, long-range, and dynamic chemical interactions present in our system. More sophisticated nonequilibrium models will be explored in future work.

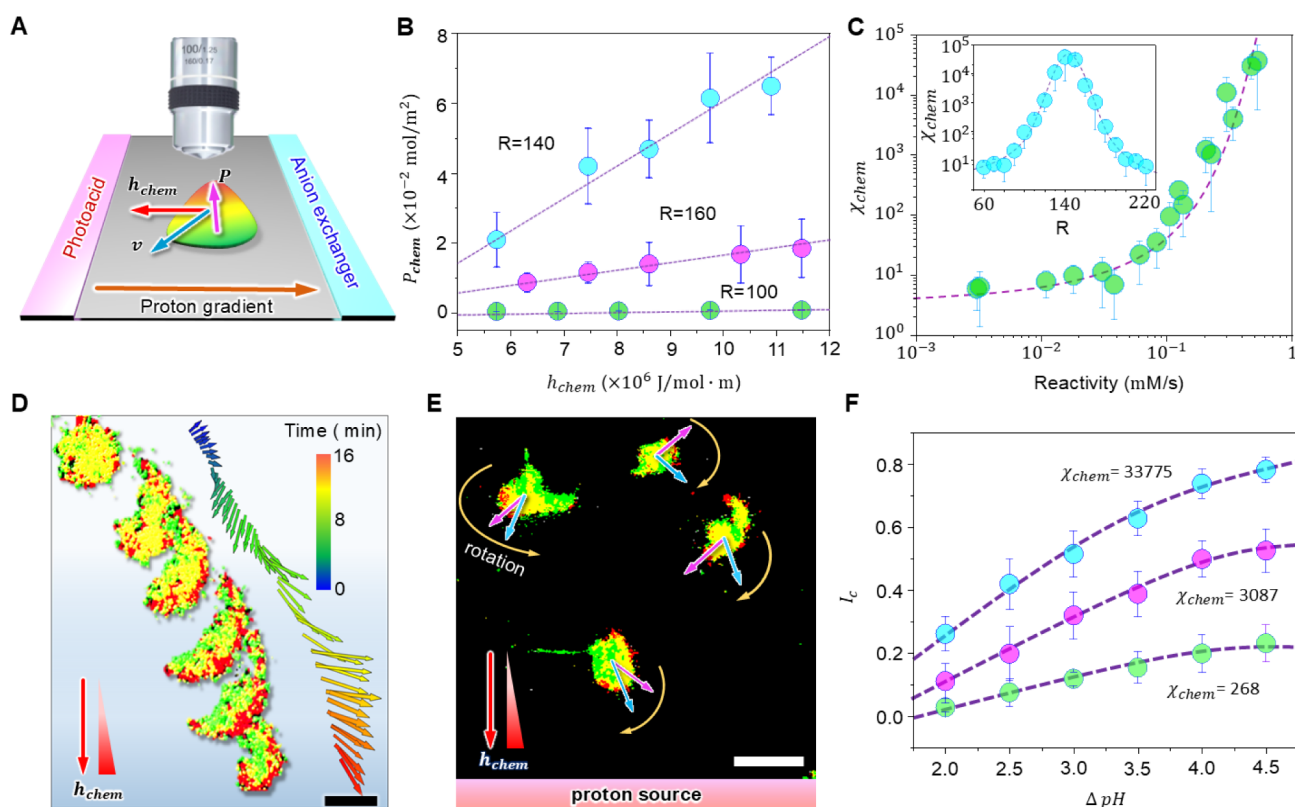


Figure 4. Chemical amplification and collective chemotaxis of the ZGO-SPS active swarm. A) Schematic diagram of the chemotaxis perfusion cell, where the light-controllable proton gradient is generated between the proton source (photoacid) and the proton drain (anion exchanger). B) Dependence of the amplitude of clusters' polarization density P_{chem} to external field strength h_{chem} with different ZGO/SPS ratios (R). C) Dependence of χ_{chem} on the reactivity of the ZGO-SPS cluster. Inset shows the dependence of χ_{chem} on the cluster composition (R). D) The fluorescent microscope images of a polarized cluster migrating under an external chemical field h_{chem} . The arrows represent the polarization density vector \mathbf{p} , while the color of the arrows represents the time evolution, as indicated by the color bar. E) Multiple clusters showing collective chemotaxis toward the proton source. The polarization density \mathbf{P} (pink arrows) and velocity \mathbf{v} (blue arrows) of the clusters gradually rotate (yellow arrows) and align with the external chemical field h_{chem} . F) Dependence of the chemotactic index (I_c) on ΔpH for clusters with different χ_{chem} . The error bars in B, C, and F are from 5 parallel experiments. Scale bar: 100 μm (D); 250 μm (E).

As depicted in Figure 3A, we consider the active cluster composed of small ZGO-SPS chemical dipole pairs, each carrying one of the two opposite polarizations ± 1 along the direction of interest, as indicated by the up or down arrows. These dipoles interact with neighboring dipoles with coupling strength J and the external chemical field h_{chem} .

It is worth noting that although J originates from the chemical reaction and is intrinsically nonequilibrium, treating J as a pseudoequilibrium interaction is beneficial to simplify the model. Similar to the ferromagnetic and antiferromagnetic phases in the Ising model,³⁹ a long-range ferric order, with all neighboring dipoles aligned in the same direction, is expected for $J > 0$, while an antiferic order, where neighboring dipoles align in opposite directions, is expected for $J < 0$. As demonstrated by the simulation in Figure 3B (see Supporting Information for the simulation details), three ZGO-SPS pairs are initially configured in parallel, while the middle pairs deviate (dashed blue arrow) by 150° (top image) and 30° (bottom image), representing the small and large fluctuations, respectively. As shown by the flow direction indicated by the red arrows, the phoretic flow induced by the chemical reaction consistently aligns the ZGO rod toward parallel alignment (Figure S9), suggesting $J > 0$ in our system. The overall cluster polarization p_{chem} can be expressed as the ensemble of all individual dipoles in the cluster as $p_{\text{chem}} = nP_0\bar{p}$, where n is the

number of dipole pairs, P_0 is the chemical dipole moment of an individual dipole (which scales with the reaction rate), and \bar{p} represents the mean orientation along the polarized direction with $-1 \leq \bar{p} \leq 1$.

The effective mean-field Helmholtz free energy (F_{MF}) of the system can be written as:

$$\frac{F_{\text{MF}}(\bar{p}, J)}{k_{\text{B}}T} \approx \frac{1}{2} \left(1 - \frac{Jz}{k_{\text{B}}T} \right) \bar{p}^2 + \frac{1}{12} \bar{p}^4 \quad (1)$$

where k_{B} is the Boltzmann constant, T is the system temperature, and z is the coordination number (see Supporting Information for detailed derivation). As shown in Figure 3C, as J gradually increases, the free energy minimum splits and shifts away from zero, corresponding to a phase transition from the disordered state to a long-range ordered state at the critical exchange strength $J_c = \frac{k_{\text{B}}T}{z}$, corresponding to $\frac{\partial^2 F_{\text{MF}}}{\partial \bar{p}^2} = 0$. The system responds markedly differently to external fields before and after the phase transition. As shown in Figure 3D, a constant external chemical field ($h_{\text{chem}} = \nabla \mu_i$) is applied to the system with increasing J , where J_1, J_2 are smaller than J_c , while J_3, J_4 are greater than J_c . With smaller J , the single free energy minimum is only slightly biased with h_{chem} , while under the aligned state ($J > J_c$), the \bar{p} associated with the free energy

minimum significantly deviates from zero, leading to a gigantic chemical polarization $p_{\text{chem}} = P_0 \bar{p}$.

Analogous to the Ising model treatment for ferromagnetic systems, the polarization can be expressed as a function of the exchange strength J and the applied chemical field h_{chem} :

$$\bar{p} = \tanh \left[\frac{1}{k_B T} (P_0 h_{\text{chem}} + z J \bar{p}) \right] \quad (2)$$

As J scales quadratically with the reaction rate as $J = a v_r^2$, while P_0 scales linearly with chemical reaction rate $v_r = b P_0$, where a and b are constants, the overall cluster chemical dipole p_{chem} should be correlated with the reaction rate v_r as:

$$p_{\text{chem}} = \frac{v_r}{b} \tanh \left[\frac{1}{k_B T} \left(\frac{v_r h_{\text{chem}}}{b} + a b z v_r p_{\text{chem}} \right) \right] \quad (3)$$

which predicts a phase transition at a critical reaction rate $v_{\text{critical}} = \sqrt{\frac{k_B T}{a z}}$ and the corresponding critical chemical dipole (p_{critical}) as $v_{\text{critical}} = b p_{\text{critical}}$. Figure 3E shows the continuous phase transition described by eq 3 in the absence of an external field h_{chem} , which is corroborated by our experimental results in Figure 3F. Here, the mean polarization density $\langle P \rangle$ of clusters is measured at different colloidal compositions, and a similar transition is observed at a critical reactivity $v_{\text{critical}} \approx 0.4$ mM/s.

2.3. Chemical Signal Amplification with Ferrochemical Clusters. In ferromagnetic materials, the external magnetic field can be amplified by the rearrangement of constituent magnetic dipoles.^{48,49} Analogously, ferrochemically active clusters can amplify weak chemical fields through their chemical polarization. Importantly, this chemical amplification is selective: only the chemical mediator involved in the exchange reaction is sensed and amplified, enabling active swarms to track specific chemical signals. To quantify the chemical amplification capability of the ZGO-SPS active clusters, we established a controllable proton gradient within a chemotaxis perfusion cell. A microfluidic channel equipped with a light-controllable proton source (photoacid) and a proton drain (anion exchange resin) (Figure 4A) was used to generate a well-controlled chemical field $h_{\text{chem}} = -RT \frac{\nabla [\text{H}^+]}{[\text{H}^+]}$, as defined in Table 1. The resin releases OH^- via anion exchange, neutralizing protons and maintaining a proton-depleted region (see Supporting Information for chemical details).

Assuming that the chemical dipole interacts with the external chemical field via an alignment energy $U = -p_{\text{chem}} \times h_{\text{chem}}$. The induced chemical dipole density should be proportional to both the chemical field and the chemical susceptibility, as defined in Table 1, $\chi_{\text{chem}} = \frac{p_{\text{chem}}}{P_{\text{solvent}}}$, where P_{solvent} is the polarization density of the blank solvent. As shown in Figure 4B, P_{chem} scales linearly with h_{chem} and is dependent on the ZGO/SPS ratios (R), with a larger slope observed in the high reactivity cluster ($R = 140$). As shown in Figure 4C, χ_{chem} is regulated by the ZGO/SPS composition, peaking at $R = 140$ and reaching 10^4 , consistent with the predictions of the Ising model. Here, the ion-exchange reaction rate between SPS and ZGO directly determines the effective coupling constant in the Ising model. The spatial distribution of sulfonate groups and metal ions governs the emergent chemical dipole, thereby linking molecular-level interactions to macroscopic swarm behavior.

Importantly, the chemical susceptibility χ_{chem} not only characterizes the sensitivity of the active swarm to the external chemical field but also depicts the chemical signal amplification ability, as $\chi_{\text{chem}} = \frac{p_{\text{chem}}}{P_{\text{solvent}}} = \frac{\nabla C}{\nabla C_0}$, where ∇C and ∇C_0 represent the chemical concentration gradient with and without active clusters, respectively. As χ_{chem} is primarily determined by the chemical activity, as shown in eq 3, while the chemical field is inversely proportional to the chemical concentration, as $h_{\text{chem}} = -RT \frac{\nabla C}{C}$, and the overall P_h will saturate at high field bias, the ferrochemical active colloid is more suitable for amplifying weak rather than strong chemical gradients.

2.4. Collective Chemotaxis of Polarized Clusters.

Since the ferrochemical active swarm can amplify chemical signals by aligning its polarization and self-propelled along this direction, the ZGO-SPS active colloid system serves as an ideal model for studying long-range collective chemotaxis. As shown in Figure 4D and Movie S3, within the controlled proton gradient, the polarization p of a ZGO-SPS cluster gradually aligns with the external chemical field h_{chem} and migrates toward the proton source. The observed changes in cluster size during chemotaxis (Figure 4D) are due to 3D morphological rearrangement and not dissociation. Cluster stability is maintained by reaction-induced phoretic interactions. Additionally, as shown in Movie S4, the active ZGO-SPS polarized clusters interact with each other both hydrodynamically and chemically, resulting in polarization alignment and cluster merging, as larger clusters absorb neighboring smaller clusters and dispersed particles via attractive diffusiophoresis. When multiple clusters are present in the proton gradient, the entire cluster system becomes highly dynamic, with the polarization direction exhibiting significant fluctuations. Consequently, the overall polarization P and velocity v tend to align, resulting in collective chemotaxis toward the proton source, as shown in Figure 4E and Movie S5. Chemotactic response persists for up to 2 h, after which coalescence and gradient depletion gradually reduce collective migration. It is important to note that the chemical gradient applied in these experiments is very weak; neither ZGO nor SPS alone is able to induce a noticeable chemotactic response (see Supporting Information for control experiment details). While the spontaneous polarization and chemotactic migration observed in our ZGO-SPS clusters bear resemblance to collective alignment and flocking phenomena described by the Vicsek model and its variants,^{50,51} the physical basis of our system is fundamentally different. In standard Vicsek-type models, alignment is local and is based on particle velocities. In contrast, our system's polarization emerges from nonreciprocal, long-range phoretic interactions mediated by dynamically generated chemical fields, leading to chemical amplification and feedback-driven symmetry breaking.

For microorganisms, the chemotactic index (I_c)^{52,53} was usually applied to quantify the ability of chemotaxis. In our experiment, the ZGO-SPS colloid mixture with various chemical susceptibility χ_{chem} (adjusted by the ZGO/SPS ratio) was introduced inside the perfusion cell with a controlled pH gradient (ΔpH). As the active colloids eventually aggregate to either side of our chemical gradient cell (Figure 4A), we define $I_c = \frac{N_s - N_d}{\text{Total number of particles}}$, where N_s and N_d are the number of colloid particles aggregated at the proton source and drain, respectively. In this study, the I_c ranges from 0 to 1, with 0 meaning no chemotaxis and 1

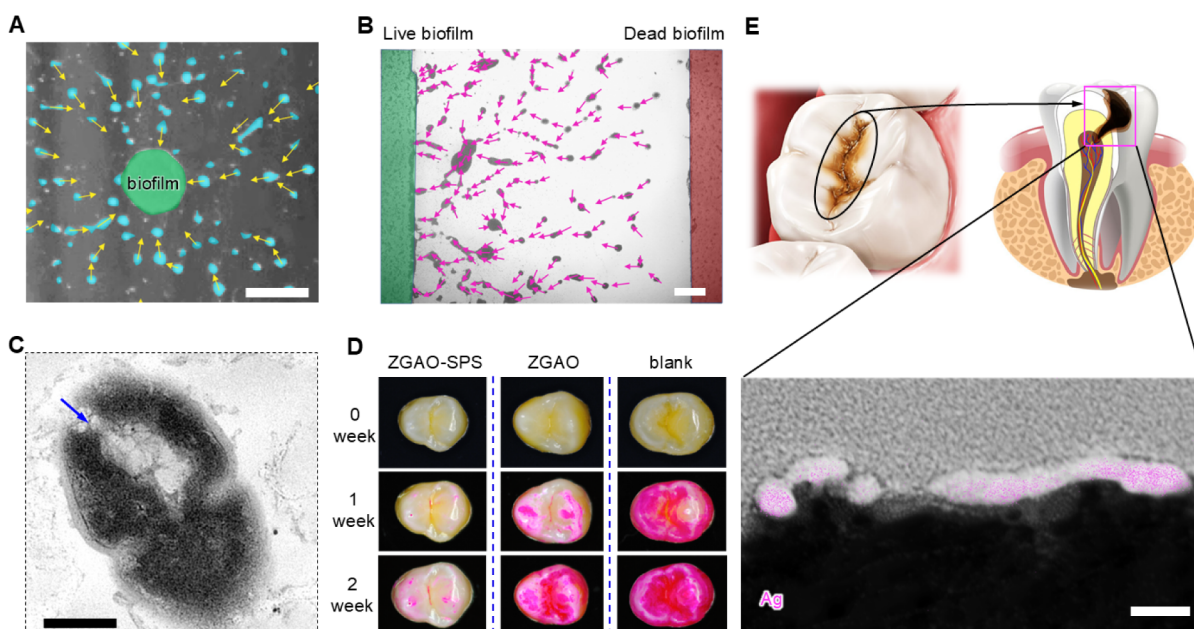


Figure 5. Antibiofilm effect of the ZGAO-SPS active colloid. A) Photo of the macroscopic chemotactic migration of the active clusters (blue) toward the biofilm (green). B) Optical microscope image shows the swarm chemotaxis toward live *S. mutans* biofilm. The green and red strips represent live and dead biofilm, respectively. C) Transmission Electron Microscopy (TEM) images of *S. mutans* bacteria treated with a ZGAO-SPS mixture, showing the bacterial membrane destruction (blue arrow). D) Comparison of consecutive images of teeth with different treatments from 0 to 2 weeks, where teeth stained with plaque stains revealed biofilm (red) on the tooth surfaces. E) Illustration of pits and fissures on the tooth and potential tooth decay by *S. mutans*. Scanning TEM image of a dental slice from the deep pit and fissure after swarm treatment. The elemental mapping shows the presence of silver in the tooth pit. Scale bars: 3 mm (A); 500 μm (B); 500 nm (C); 100 nm (E).

representing complete chemotaxis. As illustrated in Figure 4F, I_c grows with the ΔpH and is enhanced with χ_{chem} . In addition, to quantitatively assess the behaviors of colloids during collective chemotaxis, we measured the propulsion velocities of ZGO-SPS clusters at optimal composition (ZGO/SPS = 140), which revealed a mean propulsion velocity of $5.2 \pm 0.8 \mu\text{m/s}$ and is consistent with, and in some cases exceeds, velocities reported for similar ion-exchange-driven colloidal systems.^{54–57} The enhanced motility of the binary clusters directly reflects the synergistic phoretic interactions and chemical amplification described in our study. Additional velocity distributions and experimental details are provided in the Supporting Information. Furthermore, control experiments confirmed that dye labeling did not affect the colloidal activity and chemotactic response. Both labeled and unlabeled SPS beads and ZGO-SPS clusters showed statistically equivalent velocities, morphologies, and chemotactic indices (Figure S16).

It is worth noting that although the chemical signal amplification and long-range chemotaxis can theoretically be realized in laminar flow conditions, the time scale required to establish the clustering and a local chemical gradient must be shorter than the disturbances caused by the flow field. As a result, all chemotaxis experiments, as demonstrated in this study, are performed under stationary conditions. A fast-flowing environment, such as blood or cerebrospinal fluid, may not be suitable for the application of this ion-exchange-reaction-mediated chemotactic cluster.

2.5. Antibiofilm Effect by Long-Range Collective Chemotaxis. Inspired by chemotaxis in biological systems, synthetic particles with chemotactic capabilities have been employed as targeted active delivery systems.⁵⁸ However, simple chemotactic particles only provide short-range guidance

and become inefficient at distances above 500 μm .¹⁶ The remarkable enhancement of the long-range chemotactic ability in our active swarm provides a feasible method to achieve targeted delivery in a physiological environment.

As a demonstration, we doped the ZGO with 10 wt % Ag (ZGAO) as an antibacterial ingredient and applied the active swarm as a chemotactic antibiofilm agent. The detailed incorporation method of Ag and the release kinetics are provided in the Supporting Information. Comparative analyses show that Ag^+ does not alter SPS motion or cluster morphology under our experimental conditions (see Supporting Information for a detailed experimental procedure). Specifically, the active swarm was treated with *S. mutans*, a common oral bacterium that colonizes the tooth surface and is primarily responsible for dental caries and cavities.⁵⁹ Due to the excellent collective chemotaxis ability toward acid, the ZGAO-SPS active swarms can efficiently target the *S. mutans* biofilm and release silver ions locally for enhanced antibacterial efficacy. As shown in Figure 5A and Movie S6, the ZGAO-SPS suspension (ZGAO/SPS = 140) is globally dispersed in the Petri dish with an *S. mutans* biofilm in the center ($\varnothing = 3 \text{ mm}$) submerged in artificial salivary fluid, which mimics the ionic strength, composition, and pH of human saliva.⁶⁰ Owing to the selective absorption of sulfonate groups of SPS,⁶¹ the competing ions in artificial saliva do not completely suppress the ion-exchange interactions. Therefore, ZGAO-SPS clusters (blue) gradually form and migrate toward the biofilm (yellow arrows) from a distance of over 1 cm.

To further visualize the biofilm-targeting ability, the ZGAO-SPS colloid mixture was injected into an area sandwiched between two strips of live and dead *S. mutans* biofilms. As shown in Figure 5B and Movie S7, the ZGAO-SPS clusters sensed the acid signal produced and collectively migrated

toward the living biofilm. Afterward, the silver ions were locally released, which sterilized the *S. mutans*.⁶² As shown in the TEM image in Figure 5C, the bacteria treated with the active colloid exhibited distinct membrane disruption and extrusion of intracellular content, where silver particles were detected (Figure S17), confirming the effective silver delivery by the active swarm. Furthermore, the antibiofilm efficacy of the ZGAO-SPS colloid was evaluated on teeth. Comparisons were made between the biofilm mass within 3 weeks on teeth treated with active ZGAO-SPS colloid (0.1 mg/mL), ZGAO particles (0.1 mg/mL), and a blank control in artificial salivary fluid. As shown in Figure 5D, compared to ZGAO treatment, the ZGAO-SPS colloids exhibited long-range collective chemotaxis, leading to much stronger biofilm suppression efficacy. In addition, control experiments demonstrated that neither SPS alone nor ZGO-SPS (without Ag doping) exhibited significant antibiofilm effects compared with the blank control (Figure S18). Only the ZGAO-SPS clusters, which combine silver-mediated antibacterial activity with chemotactic targeting, achieved rapid and pronounced biofilm eradication.

In contrast to traditional delivery approaches that struggle to treat dental biofilms in hard-to-reach areas of teeth, such as pits and fissures, the ZGAO-SPS swarm can actively swim into narrow regions to eradicate biofilm. As shown in Figure 5E, a decayed tooth is treated with ZGAO-SPS mixture for 18 h, then the internal slice from the pit and fissure area is examined, which shows that silver is successfully delivered to these hard-to-reach locations (see Supporting Information for the detailed experimental process).

3. CONCLUSION

With chemical exchange interaction, the binary active colloid can self-polarize into active clusters, which self-propel along its polarization direction. This new phenomenon may be qualitatively explained by the simple Ising model, where the binary active mixture can be regarded as an ensemble of small chemical dipoles that form long-range order above a critical reaction rate. Adopting the metaphor of ferromagnetic and ferroelectric order, we term this new ferroic-like aggregation state as the "ferrochemical phase," which features an extraordinary ability to amplify weak chemical signals with its self-aligned chemical dipole. In our model system consisting of ZGO and SPS colloids, the binary swarm can amplify the external proton signal over 10^4 times and exhibit dramatically enhanced collective chemotactic ability. This system is exploited as an active antibacterial agent, where enhanced efficacy is realized by targeting pathogenic biofilms on tooth surfaces. Our discovery establishes a theoretical foundation for chemical amplification in artificial materials and paves the way for advanced biomedical applications for micro- and nano-robots and active matter.

■ ASSOCIATED CONTENT

SI Supporting Information

The Supporting Information is available free of charge at <https://pubs.acs.org/doi/10.1021/jacs.5c10021>.

Description of synthesis of ZGO, ZGAO, and SPS; power law-dependent coarsening of ZGO-SPS clusters; collective behavior evolution of ZGO-SPS mixture under fluorescence microscope; calculation of reactivity of ZGO-SPS mixture with various ZGO/SPS ratios;

fluorescent mapping of polarized cluster and calculation of localized ZGO/SPS ratio in polarized cluster; explanation of COMSOL simulation; calculation of the polarization density of ZGO-SPS cluster; Ising model with mean field approximation; establishment of chemical field by pH gradient; control experiment for collective chemotaxis with single component colloid of ZGO and SPS; calculation of chemotactic index; sterilization of dental biofilm by Ag-doped ZGAO-SPS active colloid, and supporting discussion (PDF)

Time-resolved coarsening of ZGO-SPS active colloid (MP4)

A polarized cluster demonstrating spring-like morphing with cyclic extension and contraction during motion (MP4)

A polarized cluster showing alignment to proton gradient (MP4)

Interaction between multiple polarized clusters (MP4)

Collective chemotaxis of ZGO-SPS clusters toward proton source along proton gradient (MP4)

Migration of ZGAO-SPS active colloid toward *S. mutans* biofilm (MP4)

Targeting migration of active colloid by tracking acid signal produced from living biofilm (MP4)

■ AUTHOR INFORMATION

Corresponding Author

Jinyao Tang – Department of Chemistry, The University of Hong Kong, Hong Kong SAR 999077, China; State Key Laboratory of Synthetic Chemistry, The University of Hong Kong, Hong Kong SAR 999077, China; Department of Chemistry, HKU-CAS Joint Laboratory on New Materials, Hong Kong SAR 999077, China; Materials Innovation Institute for Life Sciences and Energy (MILES), HKU-SIRI, Shenzhen 518055, China; orcid.org/0000-0002-0051-148X; Email: jinyao@hku.hk

Authors

Changjin Wu – Department of Chemistry, The University of Hong Kong, Hong Kong SAR 999077, China; Department of Mechanical Engineering, The University of Hong Kong, Hong Kong SAR 999077, China; Advanced Biomedical Instrumentation Centre, Hong Kong Science Park, Hong Kong SAR 999077, China

Yaxin Huang – Department of Chemistry, The University of Hong Kong, Hong Kong SAR 999077, China; School of Mechanical Engineering, Beijing Institute of Technology, Beijing 100081, China; orcid.org/0000-0003-2626-9318

Binglin Zeng – Department of Chemistry, The University of Hong Kong, Hong Kong SAR 999077, China; Department of Chemistry, HKU-CAS Joint Laboratory on New Materials, Hong Kong SAR 999077, China

Jingyuan Chen – Department of Chemistry, The University of Hong Kong, Hong Kong SAR 999077, China

Chun Hung Chu – Faculty of Dentistry, The University of Hong Kong, Hong Kong SAR 999077, China

Mingcheng Yang – Beijing National Laboratory for Condensed Matter Physics and Laboratory of Soft Matter Physics, Institute of Physics, Chinese Academy of Sciences, Beijing 100081, China; School of Physical Sciences, University of Chinese Academy of Sciences, Beijing 100081, China

Ho Cheung Shum — Advanced Biomedical Instrumentation Centre, Hong Kong Science Park, Hong Kong SAR 999077, China; Department of Chemistry and Department of Biomedical Engineering, City University of Hong Kong, Hong Kong SAR 999077, China

Complete contact information is available at:
<https://pubs.acs.org/10.1021/jacs.5c10021>

Author Contributions

[†]C.W., Y.H., and B.Z. contributed equally to this work. The manuscript was written through the contributions from all authors. All authors have given approval to the final version of the manuscript.

Notes

The authors declare no competing financial interest.

ACKNOWLEDGMENTS

The work described in this paper was partially supported by the National Key R&D Program of China (2023YFE0208700) and the MHKJFS (MHP/178/23) from the ITC of Hong Kong, a grant from the Co-funding Mechanism on Joint Laboratories with the Chinese Academy of Sciences (CAS) sponsored by the Research Grants Council of the Hong Kong Special Administrative Region, China, and the CAS (Project No. JLFS/P-701/24), the Hong Kong Research Grants Council (RGC), the Collaborative Research Fund (C7082-21G), the RGC Research Fellowship (RFS2122-7S06), the National Natural Science Foundation of China (Nos 22425205 and 22405226), and the Croucher Foundation Senior Research Fellowship (2022). This study was supported in part by the InnoHK initiative of the Innovation and Technology Commission of the Hong Kong Special Administrative Region Government. The authors also appreciate Ms. Emily R. C. Yang from HKIS for contributing artwork for concept illustration.

REFERENCES

- (1) Shellard, A.; Szabó, A.; Trepát, X.; Mayor, R. Supracellular Contraction at the Rear of Neural Crest Cell Groups Drives Collective Chemotaxis. *Science* **2018**, *362* (6412), 339–343.
- (2) Cremer, J.; Honda, T.; Tang, Y.; Wong-Ng, J.; Vergassola, M.; Hwa, T. Chemotaxis as a Navigation Strategy to Boost Range Expansion. *Nature* **2019**, *575* (7784), 658–663.
- (3) Laganenka, L.; Lee, J.-W.; Malfetheriner, L.; Dieterich, C. L.; Fuchs, L.; Piel, J.; von Mering, C.; Sourjik, V.; Hardt, W.-D. Chemotaxis and Autoinducer-2 Signalling Mediate Colonization and Contribute to Co-existence of *Escherichia coli* Strains in the Murine Gut. *Nat. Microbiol.* **2023**, *8* (2), 204–217.
- (4) Roussos, E. T.; Condeelis, J. S.; Patsialou, A. Chemotaxis in Cancer. *Nat. Rev. Cancer* **2011**, *11* (8), 573–587.
- (5) Theveneau, E.; Stevenson, B.; Scarpa, E.; Garcia, S.; Trepát, X.; Streit, A.; Mayor, R. Chase-and-Run between Adjacent Cell Populations Promotes Directional Collective Migration. *Nat. Cell Biol.* **2013**, *15* (7), 763–772.
- (6) Alert, R.; Martínez-Calvo, A.; Datta, S. S. Cellular Sensing Governs the Stability of Chemotactic Fronts. *Phys. Rev. Lett.* **2022**, *128* (14), 148101.
- (7) Tambe, D. T.; Hardin, C. C.; Angelini, T. E.; Rajendran, K.; Park, C. Y.; Serra-Picamal, X.; Zhou, E. H.; Zaman, M. H.; Butler, J. P.; Weitz, D. A.; et al. Collective Cell Guidance by Cooperative Intercellular Forces. *Nat. Mater.* **2011**, *10* (6), 469–475.
- (8) Stark, H. Artificial Chemotaxis of Self-Phoretic Active Colloids: Collective Behavior. *Acc. Chem. Res.* **2018**, *51* (11), 2681–2688.
- (9) Zöttl, A.; Stark, H. Modeling Active Colloids: From Active Brownian Particles to Hydrodynamic and Chemical Fields. *Annu. Rev. Condens. Matter Phys.* **2023**, *14* (1), 109–127.
- (10) Bishop, K. J.; Biswal, S. L.; Bharti, B. Active Colloids as Models, Materials, and Machines. *Annu. Rev. Chem. Biomol. Eng.* **2023**, *14* (1), 1–30.
- (11) Wang, Z.-H.; Chu, M.; Yin, N.; Huang, W.; Liu, W.; Zhang, Z.; Liu, J.; Shi, J. Biological Chemotaxis-Guided Self-Thermophoretic Nanoplatfrom Augments Colorectal Cancer Therapy through Autonomous Mucus Penetration. *Sci. Adv.* **2022**, *8* (26), No. eabn3917.
- (12) Chen, H.; Li, T.; Liu, Z.; Tang, S.; Tong, J.; Tao, Y.; Zhao, Z.; Li, N.; Mao, C.; Shen, J.; et al. A Nitric-Oxide Driven Chemotactic Nanomotor for Enhanced Immunotherapy of Glioblastoma. *Nat. Commun.* **2023**, *14* (1), 941.
- (13) Li, T.; Liu, Z.; Hu, J.; Chen, L.; Chen, T.; Tang, Q.; Yu, B.; Zhao, B.; Mao, C.; Wan, M. A Universal Chemotactic Targeted Delivery Strategy for Inflammatory Diseases. *Adv. Mater.* **2022**, *34* (47), 2206654.
- (14) Ghosh, C.; Ghosh, S.; Chatterjee, A.; Bera, P.; Mampallil, D.; Ghosh, P.; Das, D. Dual Enzyme-Powered Chemotactic Cross β Amyloid Based Functional Nanomotors. *Nat. Commun.* **2023**, *14* (1), 5903.
- (15) Tu, Y. Quantitative Modeling of Bacterial Chemotaxis: Signal Amplification and Accurate Adaptation. *Annu. Rev. Biophys.* **2013**, *42*, 337–359.
- (16) Tweedy, L.; Thomason, P. A.; Paschke, P. I.; Martin, K.; Machesky, L. M.; Zagnoni, M.; Insall, R. H. Seeing Around Corners: Cells Solve Mazes and Respond at a Distance Using Attractant Breakdown. *Science* **2020**, *369* (6507), No. eaay9792.
- (17) Hortelao, A. C.; Simó, C.; Guix, M.; Guallar-Garrido, S.; Julián, E.; Vilela, D.; Rejc, L.; Ramos-Cabrer, P.; Cossio, U.; Gómez-Vallejo, V.; et al. Swarming Behavior and In Vivo Monitoring of Enzymatic Nanomotors within the Bladder. *Sci. Rob.* **2021**, *6* (52), No. eabd2823.
- (18) Choi, H.; Jeong, S.-H.; Simó, C.; Bakenecker, A.; Liop, J.; Lee, H. S.; Kim, T. Y.; Kwak, C.; Koh, G. Y.; Sánchez, S.; et al. Urease-Powered Nanomotor Containing STING Agonist for Bladder Cancer Immunotherapy. *Nat. Commun.* **2024**, *15* (1), 9934.
- (19) Wang, Z.-H.; Zeng, X.; Huang, W.; Yang, Y.; Zhang, S.; Yang, M.; Liu, H.; Zhao, F.; Li, A.; Zhang, Z.; et al. Bioactive Nanomotor Enabling Efficient Intestinal Barrier Penetration for Colorectal Cancer Therapy. *Nat. Commun.* **2025**, *16* (1), 1678.
- (20) Sui, Z.; Wan, C.; Cheng, H.; Yang, B. Micro/Nanorobots for Gastrointestinal Tract. *Front. Chem.* **2024**, *12*, 1423696.
- (21) Keestra, J. M.; Carrara, F.; Stocker, R. The Ecological Roles of Bacterial Chemotaxis. *Nat. Rev. Microbiol.* **2022**, *20* (8), 491–504.
- (22) Zhang, X.; Falagan-Lotsch, P.; Murphy, C. J. Nanoparticles Interfere with Chemotaxis: An Example of Nanoparticles as Molecular “Knockouts” at the Cellular Level. *ACS Nano* **2021**, *15* (5), 8813–8825.
- (23) SenGupta, S.; Parent, C. A.; Bear, J. E. The Principles of Directed Cell Migration. *Nat. Rev. Mol. Cell Biol.* **2021**, *22* (8), 529–547.
- (24) Wheeler, J. H.; Foster, K. R.; Durham, W. M. Individual Bacterial Cells Can Use Spatial Sensing of Chemical Gradients to Direct Chemotaxis on Surfaces. *Nat. Microbiol.* **2024**, *9* (9), 2308–2322.
- (25) Wang, B.; Lu, Y. Collective Molecular Machines: Multi-dimensionality and Reconfigurability. *Nano-Micro Lett.* **2024**, *16* (1), 155.
- (26) Sun, H.; Li, M.; Li, L.; Liu, T.; Luo, Y.; Russell, T. P.; Shi, S.-R. Reconfigurable All-Liquid Constructs. *J. Am. Chem. Soc.* **2021**, *143* (10), 3719–3722.
- (27) Wu, C.; Dai, J.; Li, X.; Gao, L.; Wang, J.; Liu, J.; Zheng, J.; Zhan, X.; Chen, J.; Cheng, X.; et al. Ion-Exchange Enabled Synthetic Swarm. *Nat. Nanotechnol.* **2021**, *16* (3), 288–295.
- (28) Rana, N.; Golestanian, R. Defect Solutions of the Non-reciprocal Cahn-Hilliard Model: Spirals and Targets. *Phys. Rev. Lett.* **2024**, *133* (7), 078301.

- (29) Chiu, Y.-J.; Omar, A. K. Phase Coexistence Implications of Violating Newton's Third Law. *J. Chem. Phys.* **2023**, *158* (16), 164903.
- (30) Meredith, C. H.; Moerman, P. G.; Groenewold, J.; Chiu, Y.-J.; Kegel, W. K.; van Blaaderen, A.; Zarzar, L. D. Predator–Prey Interactions between Droplets Driven by Nonreciprocal Oil Exchange. *Nat. Chem.* **2020**, *12* (12), 1136–1142.
- (31) Osat, S.; Golestanian, R. Nonreciprocal Multifarious Self-Organization. *Nat. Nanotechnol.* **2023**, *18* (1), 79–85.
- (32) Dinelli, A.; O'Byrne, J.; Curatolo, A.; Zhao, Y.; Sollich, P.; Tailleur, J. Nonreciprocity across Scales in Active Mixtures. *Nat. Commun.* **2023**, *14* (1), 7035.
- (33) Li, Z.; Fan, Q.; Yin, Y. Colloidal Self-Assembly Approaches to Smart Nanostructured Materials. *Chem. Rev.* **2022**, *122* (5), 4976–5067.
- (34) Pan, X.; Zhang, Z.; Su, M. Colloidal Self-assembly In BioSensing Strategies for Biomarkers Diagnosis. *Innov. Mater.* **2024**, *2* (3), 100076.
- (35) Dijkstra, M.; Luijten, E. From Predictive Modelling to Machine Learning and Reverse Engineering of Colloidal Self-Assembly. *Nat. Mater.* **2021**, *20* (6), 762–773.
- (36) Zheng, J.; Chen, J.; Jin, Y.; Wen, Y.; Mu, Y.; Wu, C.; Wang, Y.; Tong, P.; Li, Z.; Hou, X.; et al. Photochromism from Wavelength-Selective Colloidal Phase Segregation. *Nature* **2023**, *617* (7961), 499–506.
- (37) Boniface, D.; Leyva, S. G.; Pagonabarraga, I.; Tierno, P. Clustering Induces Switching between Phoretic and Osmotic Propulsion in Active Colloidal Rafts. *Nat. Commun.* **2024**, *15* (1), 5666.
- (38) Yu, N.; Shah, Z. H.; Yang, M.; Gao, Y. Morphology-Tailored Dynamic State Transition in Active-Passive Colloidal Assemblies. *Research* **2024**, *7*, 0304.
- (39) Newell, G. F.; Montroll, E. W. On the Theory of the Ising Model of Ferromagnetism. *Rev. Mod. Phys.* **1953**, *25* (2), 353–389.
- (40) Klein, M. W. Temperature-Dependent Internal Field Distribution and Magnetic Susceptibility of a Dilute Ising Spin System. *Phys. Rev.* **1968**, *173* (2), 552–560.
- (41) Agudo-Canalejo, J.; Golestanian, R. Active phase separation in mixtures of chemically interacting particles. *Phys. Rev. Lett.* **2019**, *123* (1), 018101.
- (42) Speck, T.; Bialké, J.; Menzel, A. M.; Löwen, H. Effective Cahn-Hilliard equation for the phase separation of active Brownian particles. *Phys. Rev. Lett.* **2014**, *112* (21), 218304.
- (43) Saha, S.; Agudo-Canalejo, J.; Golestanian, R. Scalar active mixtures: The nonreciprocal Cahn–Hilliard model. *Phys. Rev. X* **2020**, *10*, 041009.
- (44) You, Z.; Baskaran, A.; Marchetti, M. C. Nonreciprocity as a generic route to traveling states. *Proc. Natl. Acad. Sci. U. S. A.* **2020**, *117*, 19767–19772.
- (45) Frohoff-Hülsmann, T.; Thiele, U. Nonreciprocal Cahn–Hilliard model emerges as a universal amplitude equation. *Phys. Rev. Lett.* **2023**, *131*, 107201.
- (46) Arnold, D. P.; Gubbala, A.; Takatori, S. C. Active surface flows accelerate the coarsening of lipid membrane domains. *Phys. Rev. Lett.* **2023**, *131*, 128402.
- (47) Solon, A. P.; Tailleur, J. Flocking with Discrete Symmetry: The Two-Dimensional Active Ising Model. *Phys. Rev. E* **2015**, *92* (4), 042119.
- (48) Trifunovic, L.; Pedrocchi, F. L.; Hoffman, S.; Maletinsky, P.; Yacoby, A.; Loss, D. High-Efficiency Resonant Amplification of Weak Magnetic Fields for Single Spin Magnetometry at Room Temperature. *Nat. Nanotechnol.* **2015**, *10* (6), 541–546.
- (49) Quickel, T. E.; Schelhas, L. T.; Farrell, R. A.; Petkov, N.; Le, V. H.; Tolbert, S. H. Mesoporous Bismuth Ferrite with Amplified Magnetoelectric Coupling and Electric Field-Induced Ferrimagnetism. *Nat. Commun.* **2015**, *6*, 6562.
- (50) Baconnier, P.; Dauchot, O.; Démery, V.; Düring, G.; Henkes, S.; Huepe, C.; Shee, A. Self-Aligning Polar Active Matter. *Rev. Mod. Phys.* **2025**, *97* (1), 015007.
- (51) Caprini, L.; Löwen, H. Flocking without Alignment Interactions in Attractive Active Brownian Particles. *Phys. Rev. Lett.* **2023**, *130* (14), 148202.
- (52) De-Souza, E. A.; Thompson, M. A.; Taylor, R. C. Olfactory Chemosensation Extends Lifespan through TGF- β Signaling and UPR Activation. *Nat. Aging* **2023**, *3* (8), 938–947.
- (53) Kaletsky, R.; Moore, R. S.; Vrla, G. D.; Parsons, L. R.; Gitai, Z.; Murphy, C. T. C. elegans Interprets Bacterial Non-Coding RNAs to Learn Pathogenic Avoidance. *Nature* **2020**, *586* (7829), 445–451.
- (54) Niu, R.; Palberg, T. Modular Approach to Microswimming. *Soft Matter* **2018**, *14* (37), 7554–7568.
- (55) Niu, R.; Fischer, A.; Palberg, T.; Speck, T. Dynamics of Binary Active Clusters Driven by Ion-Exchange Particles. *ACS Nano* **2018**, *12* (11), 10932–10938.
- (56) Fraxedas, J.; Reguera, D.; Esplandiú, M. J. Collective Motion of Nafion-Based Micromotors in Water. *Faraday Discuss.* **2024**, *249*, 424–439.
- (57) Niu, R.; Botin, D.; Weber, J.; Reinmüller, A.; Palberg, T. Assembly and Speed in Ion-Exchange-Based Modular Phoretic Microswimmers. *Langmuir* **2017**, *33* (14), 3450–3457.
- (58) Xia, X.; Li, Y.; Xiao, X.; Zhang, Z.; Mao, C.; Li, T.; Wan, M. Chemotactic Micro/Nanomotors for Biomedical Applications. *Small* **2024**, *20* (6), 2306191.
- (59) Li, Z.-R.; Sun, J.; Du, Y.; Pan, A.; Zeng, L.; Maboudian, R.; Burne, R. A.; Qian, P.-Y.; Zhang, W. Mutanofactin Promotes Adhesion and Biofilm Formation of Cariogenic Streptococcus mutans. *Nat. Chem. Biol.* **2021**, *17* (5), 576–584.
- (60) Pytko-Polonczyk, J.; Jakubik, A.; Przeklasa-Bierowiec, A.; Muszynska, B. Artificial Saliva and Its Use in Biological Experiments. *J. Physiol. Pharmacol.* **2017**, *68* (6), 807–813.
- (61) Boyd, G.; Soldano, B. Self-Diffusion of Cations in and through Sulfonated Polystyrene Cation-Exchange Polymers. *J. Am. Chem. Soc.* **1953**, *75* (24), 6091–6099.
- (62) Koo, H.; Allan, R. N.; Howlin, R. P.; Stoodley, P.; Hall-Stoodley, L. Targeting Microbial Biofilms: Current and Prospective Therapeutic Strategies. *Nat. Rev. Microbiol.* **2017**, *15* (12), 740–755.



CAS BIOFINDER DISCOVERY PLATFORM™

ELIMINATE DATA SILOS. FIND WHAT YOU NEED, WHEN YOU NEED IT.

A single platform for relevant, high-quality biological and toxicology research

Streamline your R&D

CAS
A division of the American Chemical Society